New wideband large aperture open-ended coaxial microwave probe for soil dielectric characterization

Alex Gélinas[1,2], Bilal Filali[3], Alexandre Langlois[2,4], Richard Kelly[5], Alex Mavrovic[1,2], François Demontoux[6], and Alexandre Roy[1,2]

[1]*Centre de recherche sur les interactions bassins versants – écosystèmes aquatiques (RIVE), Université du Québec à Trois-Rivières*
[2]*Centre d'études nordiques (CEN), Université Laval*
[3]*PhyVertX Technologies Inc.*
[4]*Centre d'Applications et de Recherches en Télédétetcion (CARTEL), Université de Sherbrooke*
[5]*Department of Geography and Environmental Management, University of Waterloo*
[6]*Laboratoire de l'Intégration du Matériau au Système (IMS), Université de Bordeaux*

***Abstract*—We present a unique Open-Ended Coaxial Probe that can accurately measure the permittivity of heterogeneous materials, such as soil, due to its large aperture. The probe works at frequencies ranging from 0.5 to $18\,\mathrm{GHz}$, which is a particularly important range for microwave remote sensing applications, and more precisely the Terrestrial Snow Mass Mission (TSMM). TSMM aims at launching a new satellite equipped with a dual Ku-band radar (13.5 and $17.2\,\mathrm{GHz}$) for snow monitoring. At Ku-band frequencies, the backscattered radar signal contains information not only about the snow, but also about the soil underneath the snow. Knowing the soil permittivity will allow to better account for the soil contribution to the total radar signal and to obtain more accurate snow data such as the Snow Water Equivalent (SWE). To demonstrate the accuracy of the probe and the repeatability of the measures, calibration solutions of known permittivity were measured, and the results were compared to their theoretical values. Then, we conducted tests for approximating the penetration depth of the probe signal with dry and wet paper. Afterwards, a protocol to use the probe to compute the permittivity of soil samples in freeze/thaw cycles was developed. The permittivity of commercial sand and arctic organic soil from Iqaluktuuttiaq (Cambridge Bay, Nunavut, Canada) are presented for different relevant frequencies for microwave remote sensing applications, and for different temperatures (-20 to $20\,^{\circ}\mathrm{C}$) according to the new protocol. This paper mainly aims at presenting the probe and its potential use in microwave remote sensing applications, especially for the active Ku-band, where little research exists.**

***Index Terms*—Coaxial probe, Microwaves, Remote Sensing, Permittivity, Soil**

I. Introduction

RECENT DEVELOPMENTS in active microwave remote sensing showed the potential of Synthetic Aperture Radar (SAR) for monitoring important snow characteristics. More precisely, studies demonstrated that the SAR backscattering in the Ku-band domain (12 to $18\,\mathrm{GHz}$) is highly sensible to Snow Water Equivalent (SWE) [1]–[3]. Following SWE temporal and spatial variations where the snow coverage spans more than 6 months per year is crucial to understand hydrological cycles [4], [5], surface energy balance [6], [7] and biogeochemical cycles [4], [8], among others. Seasonal snowmelt and SWE are key in delivering freshwater for Canadians' well-being, for supporting diverse economic sectors and for sustaining ecosystems. Simultaneously, snowmelt and SWE can impact floods and drought events. The impact of these snow variables, combined with the recent SAR developments, led to the launch of a joint mission of the Canadian Space Agency (CSA) and Environment and Climate Change Canada (ECCC): the Terrestrial Snow Mass Mission (TSMM) [9], [10], which aims to launch a dual Ku-band SAR ($13.5\,\mathrm{GHz}$ and $17.2\,\mathrm{GHz}$) aboard a satellite to monitoring snow in the Northern Hemisphere. Satellite Ku-band SAR observations would offer regular high resolution (few meters) SWE data for remote locations around the globe under various meteorological conditions [11]. Ku-band radar signals have low interactions with atmospheric particles such as water vapour in clouds and are completely independent of solar radiations.

However, a lot of challenges still exist for SWE inversion using the Ku-band SAR backscatter signal. The backscattering signal is not only influenced by SWE, but also by other snowpack characteristics such as microstructure and liquid water content, and by the substrate under the snow (sea ice, fresh water ice, soil, etc.) and vegetation cover. Modelling a signal in microwave radiative transfer models such as Snow Microwave Radiative Transfer (SMRT) [12] allows to distinguish each contribution's effect, enabling SWE retrieval from the backscattering signal. Most of the models for active remote sensing backscatter operate at lower microwave frequencies ($<6\,\mathrm{GHz}$, [13]), whereas SMRT works in a frequency range that encompasses the TSMM mission dual Ku-band frequencies. SMRT was specifically designed to include parameters such as snow microstructure and substrate characteristics, but SMRT developers still note the need for more precise wave diffusion models at the snow/substrate interface [12]. The model still misrepresents the soil contribution, which brings some uncertainty in the snow signal produced [2]. To model the soil contribution to the total backscattering signal, an important parameter to understand is the soil relative permittivity (hereafter called permittivity).

Knowing the soil permittivity allows modelling the soil influence on the total signal. In current radiative transfer models targeting snow characteristics, frozen soil permittivity is often set to a constant close to that of dry soil [14], [15], due to a lack of knowledge on the spatial and temporal variability of frozen soil permittivity. Soil permittivity greatly depends on

soil water content [16] where water permittivity is relatively high ($\varepsilon' \approx 80$ at L-band) compared to dry soil ($\varepsilon' \approx 2.5$ [17]) or ice ($\varepsilon' \approx 3.2$ [18]). Having unfrozen water in the soil greatly increases the permittivity, hence modifying the soil backscattering signal. Previous work on soil dielectric properties have been made where the dielectric constant is measured as a function of either the temperature and/or the water content and the soil texture [19]–[22]. Models for soil permittivity (called dielectric mixing models, [14], [23]–[25]) have also been previously developed.

The goal of this article is thus to present a novel Open-Ended Coaxial Probe (OECP) with an operating frequency range from 0.5 to 18 GHz able to measure the permittivity of a flat material or liquid. The probe aperture (the measurement plane) is large enough to integrate a representative average permittivity over non-homogeneous soil. The experimental setup required to operate the probe is simple and easily portable, making it perfect for laboratory and field use. In this study, we present the novel OECP and its precision over its full operating range as well as tests to estimate the probe signal penetration depth. Then, liquids of known permittivity are used to compare the probe's results to theoretical values to validate the probe calibration. Finally, a protocol was developed to measure the soil permittivity in a controlled varying temperature environment (from -20 to $20\,^{\circ}\mathrm{C}$). Two different soil types (sand and arctic organic soil) were analyzed following the new protocol.

II. Theory and Methodology

A. Probe setup

The OECP used in this project was developed by PhyVertX Technologies Inc., and is an adaptation for higher frequencies of the probe described in [26]. The probe was tested on different substrates such as vegetation, snow and ice, and soil [27]–[29]. The probe is made of two conducting coaxial cylinders with a Polytetrafluoroethylene (PTFE) core akin to a coaxial cable. The inner cylinder has a $2a = 4\,\mathrm{mm}$ diameter while the outer cylinder has a $2b = 13.2\,\mathrm{mm}$ diameter (Figure 1A).

The probe aperture is large enough to measure heterogeneous material, such as soil, while being able to cover a frequency range from 0.5 GHz up to 18 GHz. To operate the OECP, we used a 1-port VNA—the R180 (0.001 to 18 GHz, frequency resolution of 50 Hz)—from Copper Mountain® Technologies. All the instruments, connectors and cables in the setup have an impedance of $50\,\Omega$ to reduce unwanted reflections. To connect the OECP (SMA connector) to the VNA (Type-N connector), using a solid adaptor allows eliminating the noise that could occur in cables or semi-rigid adaptors. The VNA was then connected to a computer and was operated by the company's RVNA software (Figure 1C). Once the setup completed, two calibrations were performed to ensure measurements accuracy: the first calibrates the cables and connectors plugged on the probe using a specific calibration kit (system calibration) and the second calibrates the probe measurement plane, i.e., probe aperture (probe calibration, see Section II-C for more details).

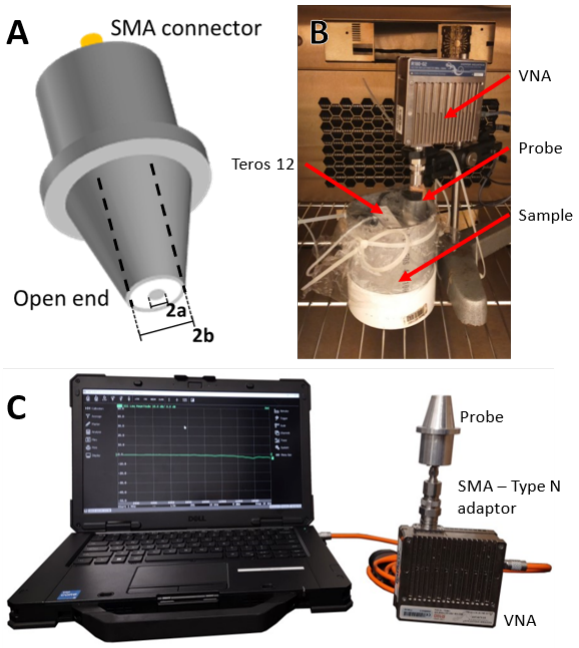

Fig. 1. **A:** OECP schematic, where the diameter of the conductive core (2a) is 4 mm and the outer diameter of the PTFE core (2b) is 13.2 mm; **B:** Experimental setup for the temperature cycle measures; **C:** VNA and OECP, connected to the computer with the operating software for the VNA

B. Probe measurement principle

To obtain the permittivity at the probe's aperture, the VNA measures the reflection coefficient ρ. The measure is then linked to the real reflection coefficient Γ through the probe's scattering parameters with the Equation 1 [30]:

$$\Gamma = \frac{\rho - S_{11}}{S_{22}\rho + S_{12}S_{21} - S_{11}S_{22}} \tag{1}$$

where the $S_{i,j}\,(i,j \in \{1,2\})$ are the probe scattering parameters. The probe calibration, detailed in Section II-C, is made to find those $S_{i,j}$ using liquids of known permittivity. Γ is also related to the admittance of both the probe (Y_0) and the material under test ($Y(\varepsilon)$) with Equation 2 [30]:

$$\Gamma = \frac{Y(\varepsilon) - Y_0}{Y(\varepsilon) + Y_0} \tag{2}$$

Finally, the medium's permittivity (ε_r) can be deduced from its admittance ($Y(K)$) with Equation 3 [31]:

$$Y(K) = \frac{\varepsilon_r Z_\nu}{\ln(a/b)} \int_0^\infty \frac{[J_0(\beta p) - J_0(\alpha p)]^2}{p\sqrt{\varepsilon_r - p^2}}\,dp \tag{3}$$

where $K = 2\pi f/c$ is the wave number in vacuum, $Z_\nu = \sqrt{\mu_0/\varepsilon_0} \approx 376.7303\,\Omega$ is the vacuum impedance, $\alpha = Ka$, $\beta = Kb$ are geometric parameters, J_0 is the zero$^{\text{th}}$ order Bessel function of the first kind and p is the integration variable.

C. Calibration

The calibration principle is based on the Short Open Load (SOL) one-port method, where measurements of known standards are compared to their theoretical values for all

three calibration standards (open, short-circuit and load). The measurements are then processed to find the $S_{i,j}$ (Equation 1) parameters of the calibration plane. To obtain accurate measurements, two calibrations are necessary: first, a system calibration at the probe connection plane and second, a probe calibration at the measurement plane. This first system calibration is performed using a S2611 calibration kit from Copper Mountain® Technologies and ensures that the VNA and the connectors and cables are calibrated. The kit includes all the necessary standards and has a $50\,\Omega$ impedance. Once the system is calibrated, the probe is connected at the end of the line and the second calibration is done. The probe calibration was designed specifically for the probe using the SOL method at the measurement plane (the aperture). The open standard corresponds to a measure in the air, the short-circuit standard was made by covering the probe with a conducting metal such as copper and the load standard was a saline (NaCl) water solution ($35\,\mathrm{ppt}$).

Using these three standards, Equation 1 can be written for each $\rho_{1,2,3}$ and $\Gamma_{1,2,3}$, where $\Gamma_{1,2,3}$ is deduced from $Y_{1,2,3}$ using Equation 2. Solving these three equations leads to a system of three equations for three unknown variables (Equation 4):

$$\begin{aligned} S_{11} &= \frac{\Gamma_1\Gamma_2\rho_3(\rho_1-\rho_2)+\Gamma_1\Gamma_3\rho_2(\rho_3-\rho_1)+\Gamma_2\Gamma_3\rho_1(\rho_2-\rho_3)}{\Gamma_1\Gamma_2(\rho_1-\rho_2)+\Gamma_1\Gamma_3(\rho_3-\rho_1)+\Gamma_2\Gamma_3(\rho_2-\rho_3)} \\ S_{22} &= \frac{\Gamma_1(\rho_2-S_{11})+\Gamma_2(S_{11}-\rho_1)}{\Gamma_1\Gamma_2(\rho_2-\rho_1)} \\ S_{12}S_{21} &= \frac{(\rho_1-S_{11})(1-S_{22}\Gamma_1)}{\Gamma_1} \end{aligned} \tag{4}$$

After the probe calibration, two test liquids were used to assess the probe calibration quality. The first test liquid was a saline solution at $20\,\mathrm{ppm}$ and the second one was methyl hydrate. Both computed permittivity were compared to the theoretical permittivity provided by Nyshadham, Sibbald, and Stuchly [30].

D. Data processing

For every measurement presented in this work, the raw data frequency ranged from 0.5 to $18\,\mathrm{GHz}$ with increments of $4\,\mathrm{MHz}$. For the probe calibration and test liquids, the permittivity was computed using the full raw data range. Afterwards, to accelerate the permittivity computation for the studied samples (wet and dry paper, wet and dry sand, and soil), the raw data was truncated so that the frequency increments were of $100\,\mathrm{MHz}$ over the range of 0.5 to $18\,\mathrm{GHz}$. This reduced the dataset size, making the computation faster while keeping enough data points to represent the permittivity's possible variation. With the permittivity computed, the results were smoothed using the rolling window average or the exponentially weighted moving average methods with a window size of $8.33\,\%$ of the total range to improve the consistency between measurements.

Since our probe covers a wide frequency range (from 0.5 to $18\,\mathrm{GHz}$), the analysis was made on specific frequencies used in SWE remote sensing. In the context of the new satellite mission concept for SWE monitoring (TSMM), the targeted frequencies were also added to the list (Table I).

TABLE I
FREQUENCY BANDS ($\pm 0.25\,\mathrm{GHz}$) ON WHICH THE AVERAGE PERMITTIVITY WAS COMPUTED WITH EXAMPLES OF RELEVANT SATELLITE-BASED SENSORS

Band	Frequency	Satellite example	Ref.
L-band	$1.5\,\mathrm{GHz}$	SMOS ($1.4\,\mathrm{GHz}$)	[32]
C-band	$6.9\,\mathrm{GHz}$	RadarSAT ($5.3\,\mathrm{GHz}$)	[33]
X-band	$10.65\,\mathrm{GHz}$	TerraSAR-X ($9.65\,\mathrm{GHz}$)	[34]
Ku-band 1	$13.5\,\mathrm{GHz}$	TSMM ($13.5\,\mathrm{GHz}$)	[9], [10]
Ku-band 2	$17.2\,\mathrm{GHz}$	TSMM ($17.2\,\mathrm{GHz}$)	

E. Probe signal penetration depth

A test using stacked paper sheets allowed estimating the probe penetration depth [35]. The process consisted in progressively stacking sheets of paper on top of a conductive metal plate (copper, high reflectivity). Every few sheets of paper, a permittivity measurement of the paper stack (low relative permittivity) was made. Once the measured permittivity remained constant for additional sheets of paper, the signal contribution from the conductive plate was assumed completely lost, yielding an estimation of the penetration depth of the probe signal. This test was repeated for dry and wet paper on $216 \times 279\,\mathrm{mm}$ ($8.5 \times 11\,\mathrm{in}$) US letter size printer paper of $0.1\,\mathrm{mm}$ thickness.

F. Soil sample characterization

The probe was used to characterize dry and wet commercial sand and arctic organic mesic soil from Cambridge Bay (Nunavut, Canada, $69.2275°$, $-104.8937°$). The arctic soil sample was collected using a cylindrical PVC soil sample holder of $5\,\mathrm{cm}$ radius and $10\,\mathrm{cm}$ height driven in the soil and excavated so the soil remained undisturbed. The wet sand and organic soil samples were exposed to a temperature ramp from -20 to $20\,°\mathrm{C}$ over 10 hours inside a Climats EX-CAL 1411-HE climatic chamber at Laboratoire de l'Intégration du Matériau au Système (IMS, Bordeaux, France). The wet sand and wet organic soil samples were placed in the convection centre of the climatic chamber (Figure 1B). A plastic wrap was used to seal the soil sample cylinder to ensure a constant soil moisture throughout all the temperature cycle. To monitor the soil moisture and the soil temperature during the tests, a thermocouple connected to the test chamber was used, as well as a Teros 12 soil moisture and temperature probe (operating frequency of $70\,\mathrm{MHz}$, METER Group, Inc. USA). The test chamber's thermocouple length is approximately $4\,\mathrm{cm}$. The thermocouple was inserted in the top layer of the soil sample.

III. RESULTS AND DISCUSSION

A. Probe calibration and test liquids

The calibration curves with the test saline solution ($20\,\mathrm{ppt}$) and methyl hydrate largely agree with the theoretical values [30] (Figure 2), with a Root Mean Squared Error (RMSE) of 1.14 and 0.94 respectively. Figure 2 also highlights the chosen frequency ranges for remote sensing applications.

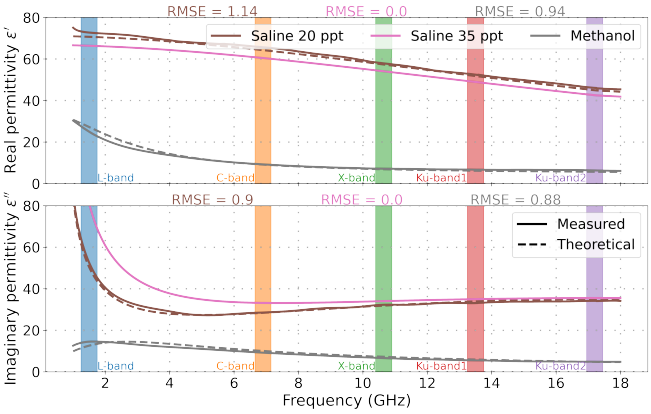

Fig. 2. Theoretical and measured permittivity of saline solution and methanol with their associated RMSE. The selected relevant frequency ranges for remote sensing applications were also highlighted

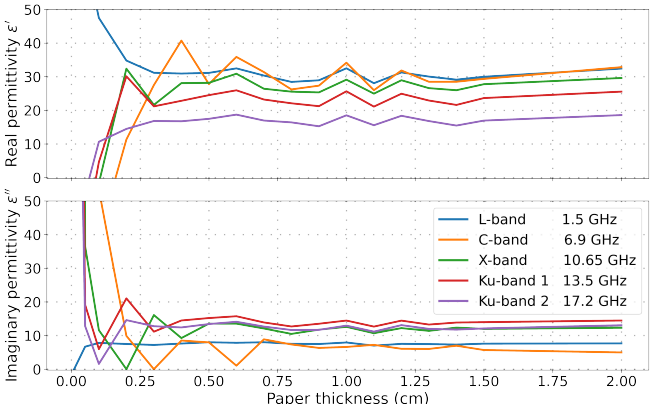

Fig. 4. Estimation of the probe signal penetration depth on soaked paper for relevant frequencies

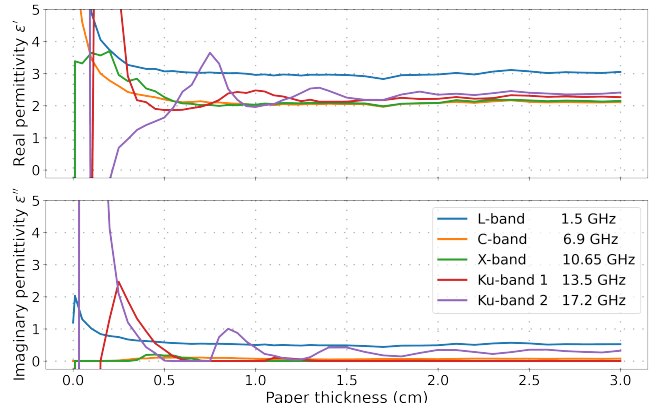

Fig. 3. Estimation of the probe signal penetration depth on dried paper for relevant frequencies

B. Signal penetration depth

For dry paper, at L-band (1.4 GHz), the curve stabilized around 0.5 cm for a value of $\varepsilon' = 3$ which is coherent with [35] who found a value around $\varepsilon' \approx 2.9$ at 1 GHz. Figure 3 also shows that the probe signal stabilizes around 0.75 cm for the other bands. Considering that the outer diameter of the probe is of 13.2 mm, the results are consistent with the rule of thumb proposed by El-rayes and Ulaby [35] that the probe penetration depth in a low loss material such as paper is approximately equal to the inside diameter of the outer conducting cylinder of the probe (see left side of figure 1, measurement 2b = 13.2 mm).

Figure 4 results for wet paper are interpreted similarly. However, since the paper's water content increases the dielectric loss, the real permittivity decreases for higher frequencies. The signal loss from the conducting copper plate noticeably happens with fewer stacked sheets than with dry paper. The probe's penetration depth in higher loss material can be estimated at around 0.3 cm. Another noticeable difference between dry and wet paper comes from the oscillations with both Ku-band frequencies between 0.5 to 1.5 cm for dry paper. These oscillations result from noise created by unwanted reflection in the dry paper medium. Indeed, the probe signal in a medium such as dry paper at high frequencies, where the wavelengths are closer in scale to the OECP cross-section, is more likely to be reflected on the sample edge and cause unwanted fluctuations in the reflection readings. At frequencies closer to L-band and C-band, where the wavelengths are larger, such unwanted reflections are negligible. In liquids such as the saline solutions used in the probe calibration process or in a moist medium such as wet paper, the probe signal is damped, preventing unwanted reflections. This signal damping also causes the penetration depth to be equal across all frequencies in the wet medium. These penetration depths mean that, to safely measure only the desired sample and not its container, a safe minimal soil depth would be over 2 cm. In the present study, the soil sample used are well over this limit with a 10 cm depth.

C. Dry sand spectrum

Since the dry sand permittivity does not vary in this range of temperature, its real and imaginary permittivity are compared to literature data from Matzler [17] (see Figure 5). In [17], the permittivity of dry sand gathered in the Sahara Desert in the frequency range of 0.245 to 6 GHz was found to be around $\varepsilon = 2.6 - [0.13, 0.012]\, j$.

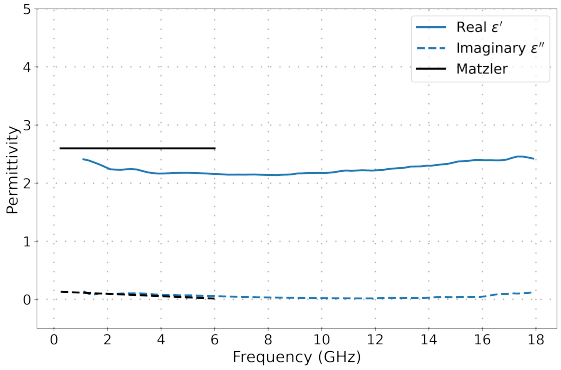

Fig. 5. Measurement of dry sand permittivity on all available frequencies compared to the measurements from Matzler [17]

Figure 5 shows that the result obtained from the probe used in the present study are consistent with what was found in the literature with a real permittivity slightly above $\varepsilon' = 2$ at lower frequencies and around $\varepsilon' = 2.6$ at the higher end. However, the permittivity presented in this paper is below the one from Matzler [17] in their study range of 0.245 to $6\,\mathrm{GHz}$. This can be explained by the grain size or physical properties of the sand [36]. Indeed, varying the density would change the permittivity, where a denser sample would have a higher permittivity since less air ($\varepsilon' = 1$) is present in the analyzed volume.

D. Freezing cycle on wet sand and organic soil

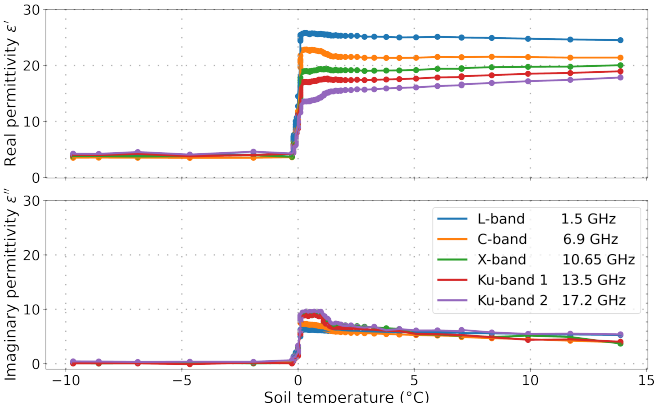

Fig. 6. Freeze/thaw cycle of sand with 25% w/w relative humidity

Figure 6 shows results of the temperature cycle on the $25\,\%$ weight/weight relative humidity sand. The graph shows that above $0\,^{\circ}\mathrm{C}$, the permittivity decreases with increasing frequency due to the sand water content, matching what was previously observed for the wet paper (Figure 4). There also seems to be a slight temperature dependency for the Ku-1- and Ku-2- bands where the permittivity increases as temperature rises. This increase is due to the variation of the water permittivity as a function of temperature [37]. At temperatures lower than $0\,^{\circ}\mathrm{C}$, a sharp decrease in permittivity followed by a plateau is observed, where all frequencies are approximately at the same value (around $\varepsilon' = 5$).

Figure 7 shows the permittivity for an arctic organic soil sample (Cambridge Bay). This sample also seems to show a greater temperature dependency above $0\,^{\circ}\mathrm{C}$ for the X- and both Ku-bands than the commercial sand where the permittivity increases with the temperature. At $15\,^{\circ}\mathrm{C}$, the permittivity of the organic soil sample for the multiple highlighted frequencies converges around $\varepsilon' = 20$, while the sand sample permittivity is more spread at the same temperature. The below $0\,^{\circ}\mathrm{C}$ permittivity also drops sharply, then plateaus when the water inside the sample is completely frozen at a value around $\varepsilon' = 5$, like the commercial sand.

Table II shows the average real permittivity of each plateau when the sample is either completely frozen or completely thawed. The uncertainty on the numbers presented in the table comes from a standard deviation from the average. The presented values can be used to parametrize radiative transfer models to compute brightness temperature or backscattering coefficients for remote sensing applications.

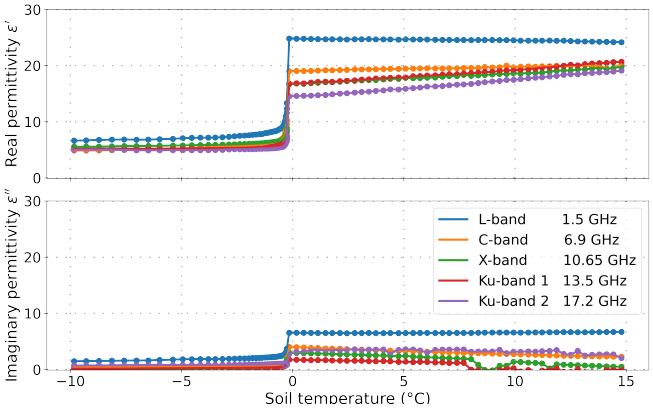

Fig. 7. Freeze/thaw cycle of wet organic mesic soil

TABLE II
MEAN REAL PERMITTIVITY OF THE FROZEN ($\mathrm{T} \leq -0.5\,^{\circ}\mathrm{C}$) AND THAWED ($\mathrm{T} \geq 0.5\,^{\circ}\mathrm{C}$) SAMPLE FOR EACH RELEVANT BAND FREQUENCIES

	Wet sand		Organic soil	
	Frozen	Thawed	Frozen	Thawed
L-band (1.5 GHz)	4.03 ± 0.04	25.3 ± 0.2	7.6 ± 0.6	24 ± 2
C-band (6.9 GHz)	3.52 ± 0.02	21.7 ± 0.3	5.8 ± 0.5	19 ± 2
X-band (10.65 GHz)	3.85 ± 0.09	19.2 ± 0.2	6.1 ± 0.3	17 ± 2
Ku-band 1 (13.5 GHz)	4.1 ± 0.2	17.5 ± 0.2	5.4 ± 0.2	17 ± 2
Ku-band 2 (17.2 GHz)	4.3 ± 0.2	15.5 ± 0.5	5.1 ± 0.2	15 ± 2

E. Potential applications for satellite missions

Our unique Open-Ended Coaxial Probe has a large aperture allowing repeatable and precise permittivity measurements of heterogeneous materials while having a frequency band ranging from 0.5 to $18\,\mathrm{GHz}$. The permittivity measurements of the wet commercial sand and of the arctic organic soil sample presented in this work vary greatly whether the soil is frozen or unfrozen, and between the highlighted frequency bands above $0\,^{\circ}\mathrm{C}$. This has a special importance for TSMM, where the soil effect on the snow water equivalent inversion from Ku-band SAR is still misunderstood [2], [3]. Furthermore, at Ku-band, the possible variability of the frozen soil permittivity due to the soil texture and composition, especially for arctic organic soil, is undetermined. Some studies also show the effect of the zero-curtain [38], [39] in arctic and boreal forest soils, where the soil under a snowpack is not completely frozen, which can greatly influence the permittivity, hence the backscattering signal.

To follow up this calibration and characterization work with the OECP, we plan on applying the freezing/thawing protocol presented above to an array of soil from different places to analyze the permittivity as a function of the soil texture, organic matter percentage, temperature and humidity. The database created with these soil characterization will then be used to produce a wideband permittivity model spanning the whole probe range.

IV. Conclusion

In this paper, we presented a novel Open-Ended Coaxial Probe that can measure the permittivity of a heterogeneous sample over a large frequency band (0.5 to $18\,\mathrm{GHz}$), which is especially relevant for microwave remote sensing. Here, we chose to only present the results for relevant satellite-based remote sensing sensor frequencies that are commonly used for snow monitoring. The probe calibration shows its reliability over all the 0.5 to $18\,\mathrm{GHz}$ range with minimal errors (RMSE ≈ 1). Tests on dry and wet stacked paper were used to determine that the penetration depth of the probe signal is between 0.5 to $0.75\,\mathrm{cm}$ depending on the frequency for the dry paper and around $0.3\,\mathrm{cm}$ for wet paper. The probe was also used to measure the permittivity spectrum of dry sand (commercial) and the values were compared to other studies found in the literature. Wet commercial sand and wet organic mesic soil (Cambridge Bay, Nunavut, Canada) samples were subjected to a temperature ramp varying from -20 to $20\,^{\circ}\mathrm{C}$. Both samples showed comparable permittivity/temperature curves where the frozen permittivity was around $\varepsilon' = 5$ and the thawed permittivity was around $\varepsilon' = 20$.

Further work using the probe is underway. The OECP permittivity measurements will be used to develop a large band soil permittivity model using the soil composition, humidity and temperature as input. Such a model can be used alongside radiative transfer models like Snow Microwave Radiative Transfer to compute the emission or backscattering contributions of different surfaces in Snow Water Equivalent retrieval algorithms. This permittivity model will also be tested on real-world data coming from the CryoSAR project. Defining better soil contribution to the total backscattering signal at Ku-band frequencies will improve the understanding of the relationship between snow microstructure, snow height and snow density in the SWE inversion models that will be used in the Terrestrial Snow Mass Mission.

V. Acknowledgement

The authors acknowledge the support of the Canadian Space Agency (19FAWATA23) and the Environment and Climate Change Canada team for their help. We also thank the Natural Sciences and Engineering Research Council of Canada (NSERC), Mitacs Globalink and the Bureau des relations internationales (BRI) of the Université du Québec à Trois-Rivières for funding this project. A special thank goes to Jean-Yves Delatage (U-Bordeaux) for his support during the soil freeze/thaw cycle analysis.

References

[1] J. Shi, C. Xiong, and L. Jiang, "Review of snow water equivalent microwave remote sensing," *Science China Earth Sciences*, vol. 59, no. 4, pp. 731–745, 2016.

[2] J. King, C. Derksen, P. Toose, *et al.*, "The influence of snow microstructure on dual-frequency radar measurements in a tundra environment," *Remote Sensing of Environment*, vol. 215, pp. 242–254, 2018.

[3] N. Rutter, M. J. Sandells, C. Derksen, *et al.*, "Effect of snow microstructure variability on Ku-band radar snow water equivalent retrievals," *The Cryosphere*, vol. 13, no. 11, pp. 3045–3059, 2019.

[4] T. Zhang, "Influence of the seasonal snow cover on the ground thermal regime: An overview," en, *Reviews of Geophysics*, vol. 43, no. 4, 2005.

[5] O. Aygün, C. Kinnard, and S. Campeau, "Impacts of climate change on the hydrology of northern midlatitude cold regions," en, *Progress in Physical Geography: Earth and Environment*, vol. 44, no. 3, pp. 338–375, 2020.

[6] J. Cohen and D. Entekhabi, "The influence of snow cover on northern hemisphere climate variability," *Atmosphere-Ocean*, vol. 39, no. 1, pp. 35–53, 2001.

[7] J. E. Box, W. T. Colgan, T. R. Christensen, *et al.*, "Key indicators of Arctic climate change: 1971–2017," en, *Environmental Research Letters*, vol. 14, no. 4, p. 045 010, 2019.

[8] P. Grogan and S. Jonasson, "Ecosystem CO2 production during winter in a Swedish subarctic region: The relative importance of climate and vegetation type," en, *Global Change Biology*, vol. 12, no. 8, pp. 1479–1495, 2006.

[9] C. Derksen, J. Lemmetyinen, J. King, *et al.*, "A dual-frequency ku-band radar mission concept for seasonal snow," Tech. Rep. providing, 2019.

[10] C. Garnaud, S. Bélair, M. L. Carrera, *et al.*, "Quantifying snow mass mission concept trade-offs using an observing system simulation experiment," *Journal of Hydrometeorology*, vol. 20, no. 1, pp. 155–173, 2019.

[11] Y.-L. S. Tsai, A. Dietz, N. Oppelt, and C. Kuenzer, "Remote Sensing of Snow Cover Using Spaceborne SAR: A Review," en, *Remote Sensing*, vol. 11, no. 12, p. 1456, 2019.

[12] G. Picard, M. Sandells, and H. Löwe, "SMRT: An active–passive microwave radiative transfer model for snow with multiple microstructure and scattering formulations (v1.0)," English, *Geoscientific Model Development*, vol. 11, no. 7, pp. 2763–2788, 2018.

[13] N. Longepe, S. Allain, L. Ferro-Famil, E. Pottier, and Y. Durand, "Snowpack Characterization in Mountainous Regions Using C-Band SAR Data and a Meteorological Model," *IEEE Transactions on Geoscience and Remote Sensing*, vol. 47, no. 2, pp. 406–418, 2009.

[14] M. T. Hallikainen, F. T. Ulaby, M. C. Dobson, M. A. El-rayes, and L.-k. Wu, "Microwave Dielectric Behavior of Wet Soil-Part 1: Empirical Models and Experimental Observations," *IEEE Transactions on Geoscience and Remote Sensing*, vol. GE-23, no. 1, pp. 25–34, 1985.

[15] Y. H. Kerr, P. Waldteufel, P. Richaume, *et al.*, "The SMOS Soil Moisture Retrieval Algorithm," *IEEE Transactions on Geoscience and Remote Sensing*, vol. 50, no. 5, pp. 1384–1403, 2012.

[16] G. C. Topp, J. L. Davis, and A. P. Annan, "Electromagnetic determination of soil water content: Measurements in coaxial transmission lines," en, *Water Resources Research*, vol. 16, no. 3, pp. 574–582, 1980.

[17] C. Matzler, "Microwave permittivity of dry sand," *IEEE Transactions on Geoscience and Remote Sensing*, vol. 36, no. 1, pp. 317–319, 1998.

[18] C. Matzler and U. Wegmuller, "Dielectric properties of freshwater ice at microwave frequencies," en, *Journal of Physics D: Applied Physics*, vol. 20, no. 12, p. 1623, 1987.

[19] J. Cihlar and F. T. Ulaby, "Dielectric properties of soils as a function of moisture content," Tech. Rep. NASA-CR-141868, 1974, NTRS Author Affiliations: Kansas Univ. Center for Research, Inc. NTRS Document ID: 19750018483 NTRS Research Center: Legacy CDMS (CDMS).

[20] P. Hoekstra and A. Delaney, "Dielectric properties of soils at UHF and microwave frequencies," en, *Journal of Geophysical Research (1896-1977)*, vol. 79, no. 11, pp. 1699–1708, 1974.

[21] P. P. Bobrov, A. V. Repin, and O. V. Rodionova, "Wideband Frequency Domain Method of Soil Dielectric Property Measurements," *IEEE Transactions on Geoscience and Remote Sensing*, vol. 53, no. 5, pp. 2366–2372, 2015.

[22] H. Kabir, M. J. Khan, G. Brodie, *et al.*, "Measurement and modelling of soil dielectric properties as a function of soil class and moisture content," *Journal of Microwave Power and Electromagnetic Energy*, vol. 54, no. 1, pp. 3–18, 2020.

[23] M. C. Dobson, F. T. Ulaby, M. T. Hallikainen, and M. A. El-rayes, "Microwave Dielectric Behavior of Wet Soil-Part II: Dielectric Mixing Models," *IEEE Transactions on Geoscience and Remote Sensing*, vol. GE-23, no. 1, pp. 35–46, 1985.

[24] V. L. Mironov, L. G. Kosolapova, and S. V. Fomin, "Physically and mineralogically based spectroscopic dielectric model for moist soils," *IEEE Transactions on Geoscience and Remote Sensing*, vol. 47, no. 7, pp. 2059–2070, 2009.

[25] L. Zhang, T. Zhao, L. Jiang, and S. Zhao, "Estimate of Phase Transition Water Content in Freeze–Thaw Process Using Microwave Radiometer," *IEEE Transactions on Geoscience and Remote Sensing*, vol. 48, no. 12, pp. 4248–4255, 2010.

[26] B. Filali, F. Boone, J. Rhazi, and G. Ballivy, "Design and Calibration of a Large Open-Ended Coaxial Probe for the Measurement of the Dielectric Properties of Concrete," *IEEE Transactions on Microwave Theory and Techniques*, vol. 56, no. 10, pp. 2322–2328, 2008.

[27] A. Mavrovic, A. Roy, A. Royer, *et al.*, "Dielectric characterization of vegetation at L band using an open-ended coaxial probe," *Geoscientific Instrumentation, Methods and Data Systems*, vol. 7, no. 3, pp. 195–208, 2018.

[28] A. Mavrovic, J.-B. Madore, A. Langlois, A. Royer, and A. Roy, "Snow liquid water content measurement using an open-ended coaxial probe (OECP)," *Cold Regions Science and Technology*, vol. 171, p. 102 958, 2020.

[29] A. Mavrovic, R. P. Lara, A. Berg, F. Demontoux, A. Royer, and A. Roy, "Soil dielectric characterization during freeze–thaw transitions using l-band coaxial and soil moisture probes," *Hydrology and Earth System Sciences*, vol. 25, no. 3, pp. 1117–1131, 2021.

[30] A. Nyshadham, C. L. Sibbald, and S. S. Stuchly, "Permittivity measurements using open-ended sensors and reference liquid calibration-an uncertainty analysis," *IEEE Transactions on Microwave Theory and Techniques*, vol. 40, no. 2, pp. 305–314, 1992.

[31] J. Galejs, *Antennas in Inhomogeneous Media*. Elsevier Science & Technology, 1969, p. 294.

[32] Y. H. Kerr, P. Waldteufel, J.-P. Wigneron, *et al.*, "The SMOS Mission: New Tool for Monitoring Key Elements ofthe Global Water Cycle," *Proceedings of the IEEE*, vol. 98, no. 5, pp. 666–687, 2010.

[33] L. C. Morena, K. V. James, and J. Beck, "An introduction to the RADARSAT-2 mission," *Canadian Journal of Remote Sensing*, vol. 30, no. 3, pp. 221–234, 2004.

[34] R. Werninghaus and S. Buckreuss, "The TerraSAR-X Mission and System Design," *IEEE Transactions on Geoscience and Remote Sensing*, vol. 48, no. 2, pp. 606–614, 2010.

[35] M. A. El-rayes and F. T. Ulaby, "Microwave Dielectric Spectrum of Vegetation-Part I: Experimental Observations," *IEEE Transactions on Geoscience and Remote Sensing*, vol. GE-25, no. 5, pp. 541–549, 1987.

[36] T. J. Schmugge, "Effect of Texture on Microwave Emission from Soils," *IEEE Transactions on Geoscience and Remote Sensing*, vol. GE-18, no. 4, pp. 353–361, 1980.

[37] U. Kaatze, "Complex permittivity of water as a function of frequency and temperature," EN, *Journal of Chemical and Engineering Data*, vol. 34, no. 4, pp. 371–374, 1, 1989.

[38] S. I. Outcalt, F. E. Nelson, and K. M. Hinkel, "The zero-curtain effect: Heat and mass transfer across an isothermal region in freezing soil," en, *Water Resources Research*, vol. 26, no. 7, pp. 1509–1516, 1990.

[39] F. Domine, M. Belke-Brea, D. Sarrazin, L. Arnaud, M. Barrere, and M. Poirier, "Soil moisture, wind speed and depth hoar formation in the Arctic snowpack," en, *Journal of Glaciology*, vol. 64, no. 248, pp. 990–1002, 2018.